Investigations on the Turbulent Wake of a Generic Space Launcher Geometry in the Hypersonic Flow Regime

D. Saile⋆, *A. Gülhan*⋆, *A. Henckels*⋆
C. Glatzer⋆⋆, *J.-H. Meiß*⋆⋆, *M. Meinke*⋆⋆, *W. Schröder*⋆⋆
⋆*Institute of Aerodynamics and Flow Technology*
German Aerospace Center, Linder Höhe, 51147 Köln, Germany
⋆⋆*Chair of Fluid Mechanics and Institute of Aerodynamics Aachen*
RWTH Aachen University, Wüllnerstraße 5a, 52062 Aachen, Germany

Abstract

The turbulent wake flow of generic rocket configurations is investigated experimentally and numerically at a freestream Mach number of 6.0 and a unit Reynolds number of $10 \cdot 10^6$. The flow condition is based on the trajectory of Ariane V at an altitude of 50 km, which is used as baseline to address the overarching tasks of wake flows in the hypersonic regime like fluid-structural coupling, reverse hot jets and base heating. Experiments using pressure transducers and high-speed schlieren measurement technique were conducted to gain insight into the local pressure fluctuations on the base and the oscillations of the recompression shock. This experimental configuration features a wedge-profiled strut orthogonally mounted to the main body. Additionally, the influence of cylindrical nozzle extensions attached to the base of the rocket is investigated, which is the link to the numerical investigations. Here, the axisymmetric model possesses a cylindrical sting support of the same diameter as the nozzle extensions. The sting support allows investigations of a undisturbed wake flow. A time-accurate zonal RANS/LES approach was applied to identify shocks, expansion waves, and the highly unsteady recompression region numerically. Subsequently, experimental and numerical results in the strut-averted region are opposed with regard to the wall pressure and recompression shock frequency spectra. For the compared configurations, experimental pressure spectra exhibit dominant Strouhal numbers at about $St_D = 0.03$ and 0.27 and the recompression shock oscillates at 0.2. In general, the numerical pressure and recompression shock fluctuations agree satisfactorily to the experimental results. The experiments with a blunt base reveal base-pressure spectra with dominant Strouhal numbers at 0.08 at the center position and 0.145, $0.21 - 0.22$ and $0.31 - 0.33$ at the outskirts of the base.

1. Introduction

At high altitudes, launch vehicles face various tasks. The unsteady recirculation zone features periodic pressure fluctuations that lead to the excitement of components, thus to dynamic loads acting in the base region. The components are exposed to reverse hot jets resulting from the transport of hot gas from the nozzle plume upstream to the base. This can cause confined hot spots, but also increases the overall thermal load on the components under consideration. Further, for supersonic projectiles Rollstin [11] determines the base drag caused by the separation of the outer flow to be up to 35% of the overall drag, which could be even higher in the case of launch vehicles having a larger base area and might excite vibrations of critical amplitude.

These considerations drive the interest to expand the understanding of the base flow physics in the hypersonic regime and offer a strong motivation of wake flow investigations. In spite of mostly simple base geometries, the flow field is highly complex, covering the interaction of the recirculation region with the separated shear layer, expansion waves and a recompression region. These aerodynamic characteristics affect the overall axial force and exhibit periodic flow phenomena. Therefore, it is of high interest to provide accurate analyses of the not yet fully understood time-dependent base flow to design reliable future space systems.

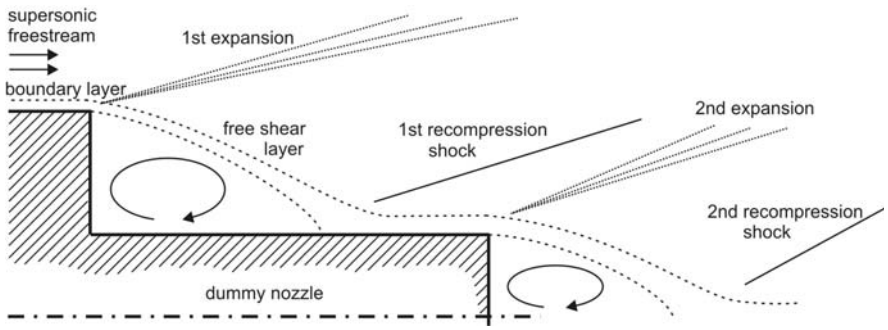

Figure 1: Schematics of the mean base flow features

A sketch of the mean flow features is given in Fig. 1. The incoming supersonic flow and the boundary layer on the surface of the model experience an abrupt geometry change at the end of the model, which results in an flow separation. The separated flow expands, meaning a deflection towards the axis takes place. A high energetic free shear layer evolves right from the edge of the base, which separates the inviscid external flow from the recirculation region downstream of the base. The shear layer is subjected to an adverse pressure gradient before reattaching on the solid surface, whereas the flow consequently realigns along the nozzle in the axial direction. This is where compression waves emanate and focus to a recompression shock. This configuration with a nozzle attachment exhibits a second stage of expansion and recompression at the rear end of the nozzle. Downstream from the nozzle, a free shear layer reattachment takes place, which essentially can also be found when no nozzle is attached to the base. Obviously, no second stage of expansion and recompression can be found when the model is held by a sting.

As a baseline for the investigations at hand, a selected stage of the Ariane V trajectory was selected. The studies simulate the launch the conditions at an altitude of 50 km, which corresponds to a freestream Mach number of 6.0 and a unit Reynolds number of $10 \cdot 10^6$. In this flow regime a less coupled fluid-structure interaction appears, while real gas effects and unsteady shock phenomena in the base region become more important.

The objective of the present paper is the experimental and numerical investigation of the turbulent wake flow with focus on unsteady flow behavior by means of base pressure fluctuations and fluctuations of the recompression shock. The advantages of both methods of investigation are exploited, and experimental and numerical results are opposed to each other. The experimental side made use of the flexibility to investigate the behavior of the wake to different nozzle extensions, whereas the numerical simulations provided detailed time-resolved data about all flow parameters in the field of interest. Another complementing aspect of the numerical investigations concerns the influence of the strut. Ottens et al. [10] showed that the base pressure decreases considerably due to a wind tunnel strut. For the numerical investigation, the axisymmetric model possesses a cylindrical sting support, which allows investigations of a less disturbed wake flow.

The experiments were conducted with Kulite pressure transducers and high-speed schlieren measurement technique. For the numerical simulations, a zonal RANS/LES approach is applied. RANS models are not capable of predicting accurate unsteady data and also fail to provide accurate results concerning the low pressure recirculation area behind the base, while the predictions of the attached flow around the main body are quite satisfactory. DNS is at the present time restricted to small Reynolds numbers and a small integration domain. Hence, RANS simulations are used to predict the attached main body flow field while LES computations are applied to the unsteady wake flow using the RANS results as inflow conditions. The turbulent viscosity of the RANS model can be used to generate physical turbulent fluctuations at the inlet of the LES domain.

2. Methods

The experiments and numerical simulations were carried out on identical generic models that only differ by the support in the flow field. Fig. 2 shows a sketch of the experimental model, called configuration A, which is supported by a strut, and Fig. 3 shows configuration B for the numerical investigations, which is supported by a sting mounted at the base of the main body. This support sting mimics the contour of a nozzle and allows for investigations of an axially undisturbed base flow.

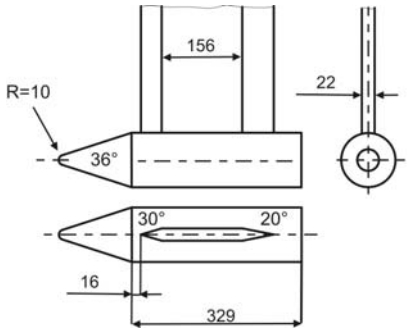

Figure 2: Geometry of the generic rocket configuration with strut support (configuration A)

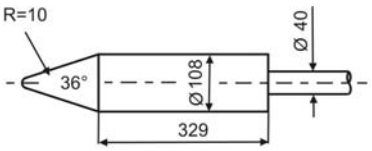

Figure 3: Geometry of the generic rocket configuration with sting support (configuration B)

The models are a representation of the Ariane V configuration with respect to the main geometrical bodies. The exterior geometry is an assembly of simple geometrical bodies. It consists of a spherical nose with a radius of 10 mm that is attached to the cylindrical main body with a diameter of $D = 108$ mm and a length of 328.6 mm via the cone with an apex angle of 36°.

The experimental wind tunnel model is shown in Fig. 4, which is equipped with a strut. The strut attached is defined by a front wedge with an apex angle of 30°, a shaft with a width of 22 mm and a length of 156 mm and rear wedge with an opening angle of 20°. The reference configuration A was modified during the experiments by mounting cylinders at the base to mimic the exterior geometry of a nozzle. No nozzle flow was applied. Nozzle lengths of $L/D = 0, 0.5, 1.0, 1.2$ were investigated. The diameter of the nozzle extension for all experiments was kept at $d/D = 0.4$, which corresponds to the diameter of the sting support for configuration B. Comparisons can be drawn to the measurements with configuration A with the attached nozzle extension.

For the experiments presented here, the H2K facility later described in Chap. 2.1 was operated at a reservoir pressure of 10 bar and a reservoir temperature of 430 K at a freestream Mach number of 6.0, which equals a unit Reynolds number of $10 \cdot 10^6\,\mathrm{m}^{-1}$. The flow conditions of the numerical simulations correspond to the experimental data.

2.1 Experimental methods

A detailed overview to the methods applied is described in [12]. Most of the measurement methods are identical. The measurements were performed in the supersonic wind tunnel H2K at the Institute of Aerodynamics and Flow Technology in the Supersonic and Hypersonic Technology Department located in Cologne. The wind tunnel H2K is a blow-down type wind tunnel equipped with a vacuum sphere to reach high Mach numbers. Six different aerodynamic testing nozzles are available for discrete Mach numbers within Mach 4.8 and 11.2. An electric heater can heat the air in the reservoir chamber up to 1100 K to adjust the Reynolds number.

In order to trigger the transition of the boundary layer to a turbulent state, four tripping configurations have been applied successively using carborundum with a grain size of 400 μm and a zigzag-tape of the same height as tripping elements. First, a ring of carborundum with a width of 5 mm was applied on the nose at 45.4 mm (conf. 1) measured from the tip of the nose along the symmetry axis. Then, a second ring was added at 201.4 mm (conf. 2) on the cylindrical main body. Later, another ring was added at 352.4 mm (conf. 3). At last, the two rings on the main body were removed and replaced by a zigzag-tape at 201.4 mm (conf. 4). After having made the experience that the tripping elements had little influence on the base-pressure behavior, the experiments presented here have been executed with tripping conf. 3 and conf. 4.

Steady and unsteady measurement techniques were applied. For the measurements concerning the boundary layer, the Pitot pressure was measured with a Pitot rake mounted at the end of the blunt base (see Fig. 5). In order to incorporate the full boundary layer thickness, the rake was elevated in a second run. Each pressure tube was connected to a 15 psi pressure scanner of Esterline Pressure Systems containing piezoresistive sensors and read with a system 8400 pressure data acquisition unit. The measurement uncertainties are 0.1% of full scale. The Pitot pressure is compared to results from RANS simulations on a two dimensional axisymmetric grid. The calculations were executed with slip and no-slip wall conditions and Spalart-Allmaras and Wilcox $k-\omega$ were chosen as turbulence models.

Figure 4: Wind tunnel model

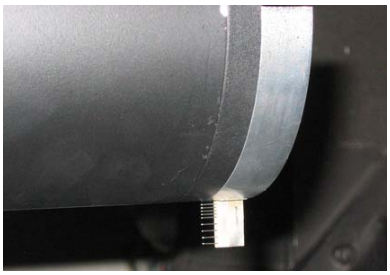

Figure 5: Pitot rake mounted on afterbody

Figure 6: Instrumentation of base with Kulites pressure transducers

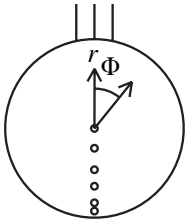

Figure 7: Radial pressure transducer arrangement

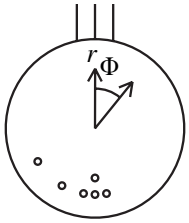

Figure 8: Reference pressure transducer arrangement

In order to measure the unsteady behavior of the recompression shock behind the base, a high-speed schlieren technique was applied using an Ultima APX-RS camera of Photron. It is equipped with a 10 bit CMOS sensor, which provides a resolution of 1024 $\times$ 1024 pixel at a frame rate of 3000 fps and a maximum frame rate of 250000 fps at a reduced resolution. The recompression shock was recorded with 10000, 16800, 20000 and 22500 fps, that resulted in 21000 to 56000 frames for spectral analysis depending on the pixel resolution. High-frequency pressure measurements were obtained with Kulite differential XCQ-080 pressure transducers, which feature typically a combined non-linearity, hysteresis and repeatability of 0.1%. Six pressure transducers with a pressure range of 0.35 bar were flush mounted in plugs of the base (see Fig. 6) where they were held in place with O-rings. The pressure reference tubes were connected to the ambient pressure of the measurement chamber. A GBM Viper system is used for the data acquisition purposes. The data was acquired over 10 s with a sampling rate of 96000 Hz. The cut-off frequency was set internally by the data acquisition system to 48000 Hz.

Additionally, infrared images were taken using the ThermaCAM SC3000 NTS camera of FLIR to gain information about the location of boundary layer transition. These infrared images show only qualitative results, which refers to the fact that the surface material of the wind tunnel model is black-painted steel, meaning that the wall material features a high temperature conductivity and an unknown emission coefficient. For this reason, the heat flux can not be determined using infrared images only and fine structures phenomena smooth out. But the qualitative temperature distribution reveals the transition location, and additionally gives insights to the disturbance effects coming from the strut holding the model.

The Kulite pressure transducers are flush-mounted on the base in two different transducer arrangements. Fig. 7 shows the radial arrangement with the transducers on the opposite side of the strut ($\Phi = 180°$) at a radius r at 0, 12, 25, 35, 45, 50 mm. Further measurements were conducted with an angle of $\Phi = 225°, 270°, 315°$. Fig. 8 displays the azimuthal arrangement where the transducers are distributed angularly at a radial distance of $r = 40$ mm at $\Phi = 170°, 180°, 190°, 210°$ and 240°. Additionally, another transducer is placed at $r = 30$ mm and $\Phi = 180°$.

The unsteady measurements from the high-speed camera and the pressure transducers were both analyzed using the fast Fourier transform algorithm (FFT). In the case of the high-speed schlieren measurements, the vertical position of the shock was gained by analyzing the intensity profile at a defined location for each image [9]. Then, the data sequence was segmented into sets of 1024 with an overlap of 50%, multiplied with a Flattop window to suppress side-lobe leakage. For the pressure transducers, segments of 8192 samples with an overlap of 50% were used in combination with a Hanning window. The spectra are given in non-dimensional frequency as Strouhal number. It is

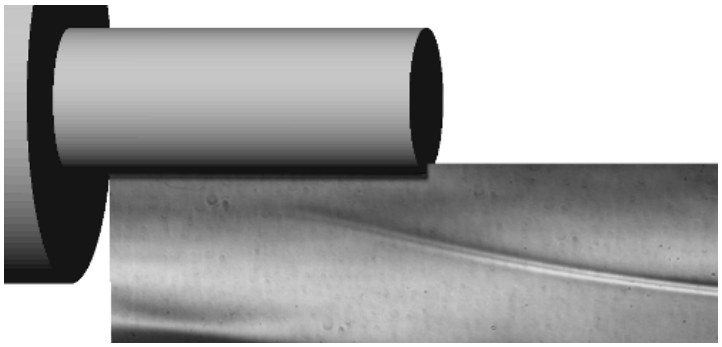

Figure 9: Standard deviation of a sequence of high-speed schlieren measurement showing the recompression shock exemplary for a nozzle length of $L/D = 1.2$ and a diameter of $d/D = 0.4$

defined as $Sr_D = fD/u_\infty$ with the frequency f, the diameter of the base D and the free stream velocity u_∞. The FFT returns a level of amplitude that is essentially dependent on the number of input values, and, hence, the level of the fluctuations does not directly represent the physical value. Yet, the relative levels can be compared.

The high-speed schlieren image sequence of the recompression shock was additionally processed by determining the standard deviation of the gray values of each pixel within the sequence. The result is an image that shows the local deviation of the shock from the mean (Fig. 9). Pixels with a lighter gray have a higher deviation from the mean than pixels with a darker gray, which was used to extract the mean location of the recompression shock.

2.2 Numerical Approach

The Navier-Stokes equations for compressible flows are solved in conservative form with a mixed central-upwind AUSM (advective upstream splitting method) scheme of second-order accuracy with low dissipation [7]. After splitting the inviscid fluxes into a convective and a pressure part and inserting the local speed of sound c, the convective part is reformulated using a Mach number weighted interpolation

$$F^c = \frac{1}{2}\left[(Ma_+ + Ma_-)(f_-^c + f_+^c) + |Ma_+ + Ma_-|\,(f_-^c - f_+^c)\right]. \tag{1}$$

The fluxes $f_\pm^c$ and the Mach number $Ma_\pm$ at the cell boundaries are determined by left and right interpolated variables obtained using the MUSCL approach according to van Leer [6]. The viscous terms are discretized by a central scheme of second-order accuracy. The temporal integration is performed by an explicit 5-stage Runge-Kutta scheme of second-order accuracy, optimized for maximum stability of a central scheme. For the calculation of the base area an LES is performed, following the monotone integrated LES (MILES) approach [2]. No explicit subgrid scale (SGS) model is implemented, but the dissipation of the numerical scheme serves as an implicit SGS model [1].

The flow around the main body is simulated using the one-equation RANS model according to Spalart and Allmaras [13]. The results of the RANS solution close to the trailing edge of the main body are used initially as inflow conditions for the base flow domain. The turbulent viscosity of the RANS model is used to generate physical turbulent fluctuations at the inlet of the LES domain [5, 15]. The Reynolds stress is reconstructed starting from a normalized stochastic velocity signal, which is disturbed by a superimposition of turbulent structures with prescribed geometrical shape and random signs and position. A body force is added to the wall-normal momentum equation on a number of control planes at different streamwise positions in order to match the turbulent flow properties of the LES with the given RANS values [4, 14]. To keep the transition zone between the RANS and LES domains small, the added synthetic turbulence accords to Jarrin *et al.* [3].

The geometry is reproduced by a structured multi-block grid (Fig. 10), which is split into two sections. One domain covers the main rocket geometry, in which the fully three-dimensional RANS simulation is carried out and the second encompasses the sting support, thus capturing the highly time-dependent base area and the wake. The 360° grid extends to physical values of 2.5 D downstream of the base shoulder in the streamwise direction and captures the oblique shock in the radial direction. The zonal overlapping zone spans up to 1 diameter upstream from the base shoulder. The grid possesses a maximum resolution of $(\Delta x^+_{wall}, \Delta r^+_{wall}, \Delta\Phi^+_{wall}) = (500, 1, 150)$ within the RANS domain and of $(\Delta x^+_{wall}, \Delta r^+_{wall}, \Delta\Phi^+_{wall}) = (50, 1, 40)$ within the LES domain with x being the streamwise, r the wall-normal, and

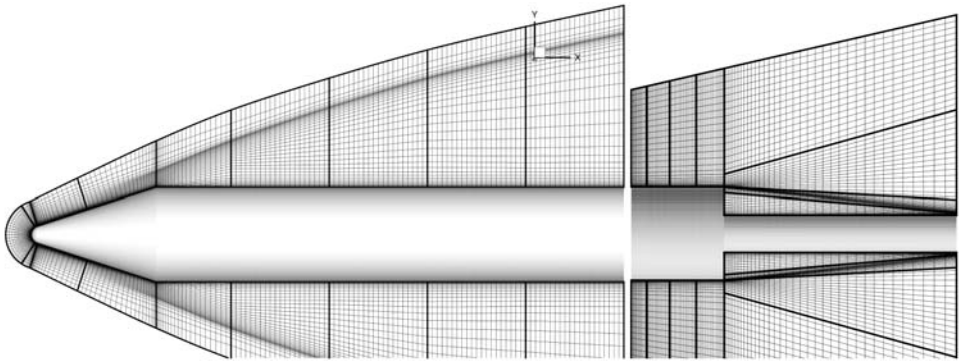

Figure 10: Computational grid for the sting support configuration

Φ the spanwise coordinate. Additional refinement is realized along the separating boundary layer and the free shear layer. The $16.2 \cdot 10^6$ grid points of the LES domain are equally distributed over 16 blocks to allow load-balancing for an efficient parallel computation.

The boundary conditions are prescribed as follows. Following a characteristics approach, at supersonic boundaries all variables are prescribed or extrapolated, respectively. At solid walls an isothermal no-slip condition is imposed, since the numerical results are compared to short time wind tunnel tests that lead to a negligible heating of the model.

Analogously to the experimental data analysis the numerical spectral analysis of unsteady pressure fluctuations on the outer surface and recompression shock movements were performed using the fast Fourier transform algorithm. The basis of the spectral analysis are formed by 1024 samples with a constant time step of $3 \cdot 10^{-5}$ s to which the Hanning window function is applied.

3. Results

The discussion of the experimental results are divided into a precursory part where the flow upstream of the base is discussed and a main part that only focuses on the base flow. An infrared image of the wind tunnel model and the Pitot pressure at the base measured by a Pitot rake is the foundation for the investigations here. In the main part, the mean location of the recompression shock as well as the corresponding spectra is presented. Last, data of the pressure fluctuations directly on the base are provided by means of spectral analysis for different nozzle extensions.

3.1 Forebody Measurements

The underlying idea of the forebody measurements is to deliver representative parameters as input parameters for numerical studies. A first impression can be gained by qualitative result of the IR-thermography Fig. 11. It shows the surface temperature of the wind tunnel model color-coded from blue to red whereas red denotes a higher temperature. Due to the perspective of the camera, the discussion of the cone is neglected. It can be seen that higher temperatures first set in right at the strut and spread angularly over the surface further downstream. At the base of the model, the temperature transition covers almost the whole cylinder. Nevertheless, lower temperatures can still be detected at the strut averted side. Within the high temperature region, streaks of higher temperatures evolve from the tip of the strut and propagate downstream of the main cylinder.

The Pitot pressure is measured at the rear end in radial direction from the model surface at the strut averted side. The results of numerical simulations are plotted in Fig. 12 for comparisons to experiments. Close to the wall between $\Delta r = 0.2$ and 3.2 mm, the numerical results with slip condition correlate with the experimental results. However, at higher radial distances, the Pitot pressure measurements tend to follow the curve given by the numerical results from the no-slip wall conditions. At about $r = 15$ mm, the Pitot pressure reaches a steady state in experiments as well as in numerics. Slight discrepancies between the two methods can be seen in the final value of the Pitot pressure. Also,

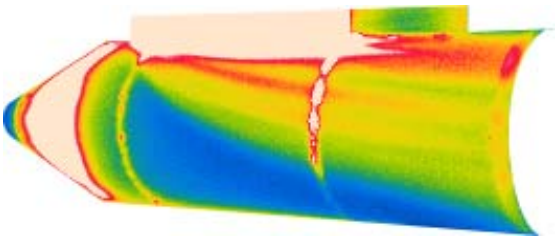

Figure 11: Infrared image showing the surface temperature of the forebody for the investigation of the boundary layer transition

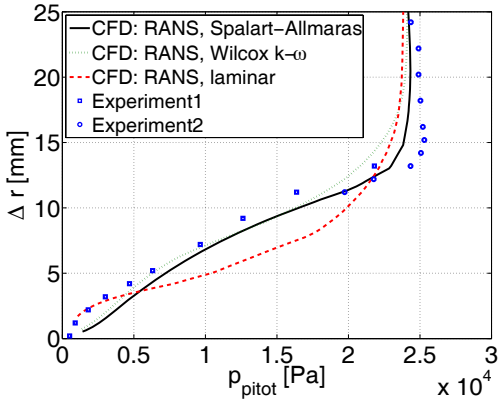

Figure 12: Experimental ($\Phi = 180°$) and numerical Pitot pressure of the boundary layer. Numerical Pitot profiles reflect a laminar boundary layer and two turbulent boundary layers based on the turbulence models Spalart-Allmaras and Wilcox $k-\omega$.

the two different runs that were necessary to gather information about the full height of the boundary layer are not completely congruent. No satisfying explanation was found for this deviation.

3.2 Base Flow Measurements

One of the most striking features of the base flow is manifested in the recompression shock. After the expansion at the rear end, the flow deviates towards the axis and causes a recompression region downstream from the base, which leads this shock. This was measured with the high-speed schlieren method and analyzed as described before concerning the mean location of the shock and plotted in Fig. 13 in x-r coordinates. The continuous lines represent the investigated nozzle extension configurations and the base is indicated along the r-axis as a thick black line. The recompression shock location is plotted as a dashed line. Nozzle extension sketch and recompression shock are plotted in the same color.

For no nozzle attachment, the fine line of the recompression shock could first be detected at about 1.1 diameter lengths downstream of the base at $r/D = 0.325$. The shock angle is 7.6°. The most outstanding observation after a applying a nozzle extension with a length of $L/D = 0.5$ refers to the kink of the shock at $x/D = 1.42$ and $r/D = 0.38$. Further upstream to that kink, the shock angle is 2.9°. Downstream to that kink, the shock location coincides with the shock location of the configuration without a nozzle. A lengthening of the nozzle extension to 1.0 causes a parallel shift of the shock location of 0.6 diameters upstream to the base. A further lengthening to 1.2 does not affect the shock location any more. The shock location of the two longest nozzle extensions coincide.

The corresponding numerical investigations differ from the experimental results. Fig. 14 shows the pressure in color codes in the same coordinate system as the graph mentioned before. The darker blue indicates a lower pressure. The experimental results for the recompression shock of the nozzle with $L/D = 1.2$ is plotted along with the numerical data. It can be seen by the pressure increase that the shock is determined to be 0.6 diameters downstream from the experimental shock location result. The shock angle shows a good match to the experimental results.

It can clearly be seen in the high-speed schlieren video that the recompression shock oscillates around its mean value. The instantaneous vertical position of the shock was extracted as described in reference [9] and subjected to its amplitude spectra. Fig. 15 shows the vertical amplitude in pixels over the Strouhal number. A arbitrary vertical location of the recompression shock was chosen since the spectra has shown to be independent to the location. The various curves (red, magenta, blue, green refer to $L/D = 0, 0.5, 1.0, 1.2$, respectively) represent the different nozzle extension lengths. A polynomial of the order 8 is fitted to the curves to give a better impression of the course. It can be seen that the peak level for all extension centers at about $St_D = 0.18 - 0.19$ independent of the nozzle extension. Fig. 16 also depicts the spectra of the recompression shock and a polynomial of the order 5, but from numerical simulations. Although only 1024 samples were used here, the polynomial shows clearly a tendency to center around $St_D = 0.18$.

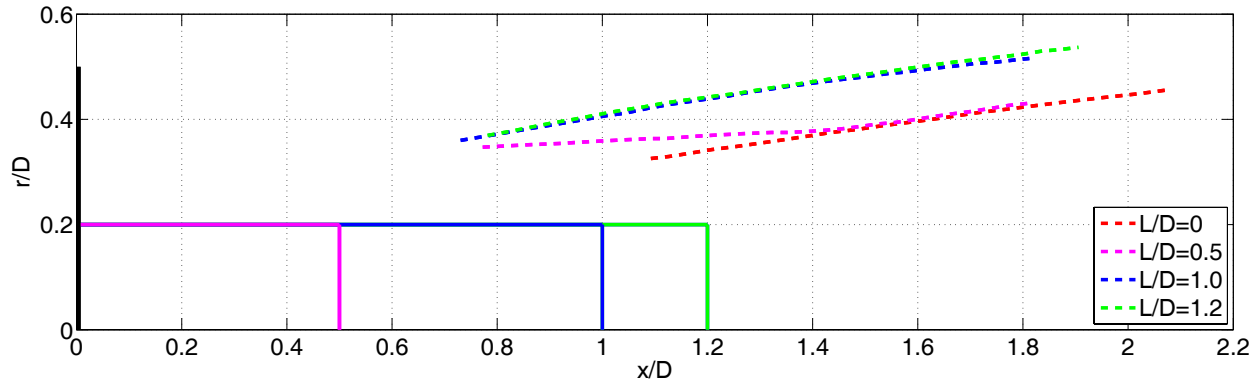

Figure 13: High-speed schlieren experimental results concerning the mean recompression shock location for different nozzle lengths L at the strut averted side ($\Phi = 180°$)

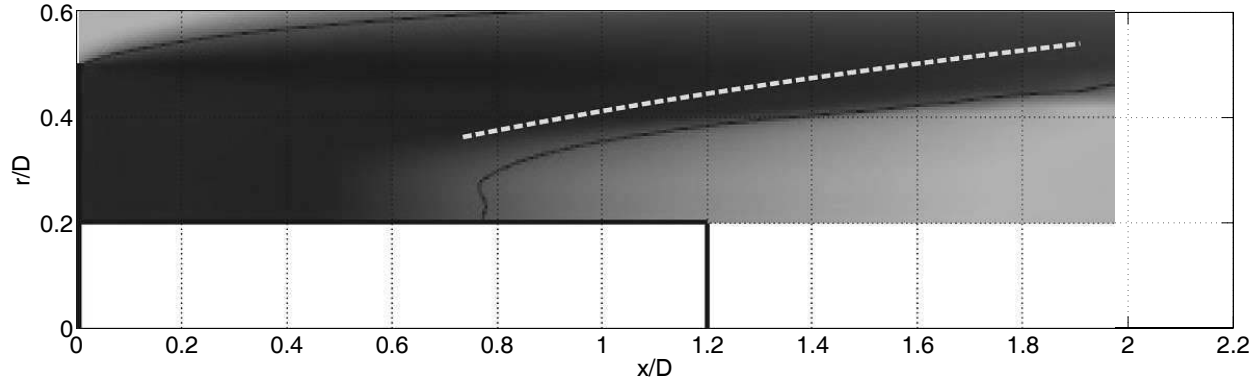

Figure 14: Numerical result concerning the mean recompression shock location in comparison to the experimental results for a nozzle extension of $L/D = 1.2$

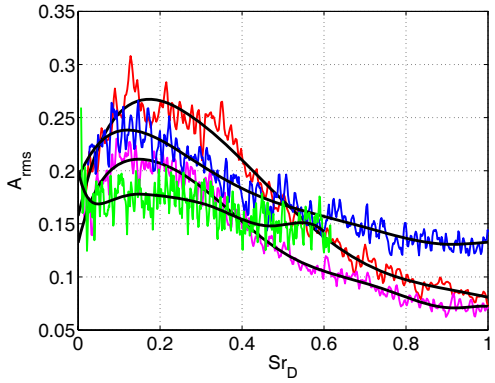

Figure 15: Experimental spectra of the recompression shock location for different nozzle extension length

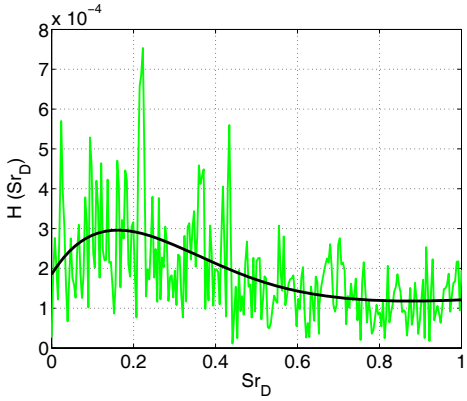

Figure 16: Numerical spectra of the recompression shock location calculated

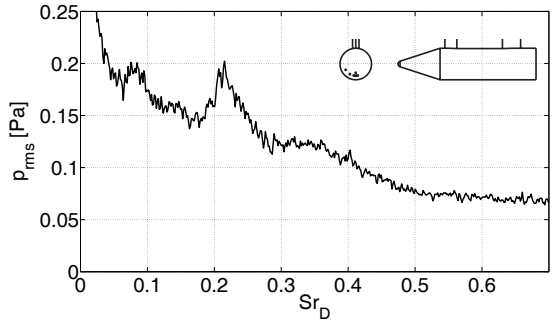

(a) Location: $r = 40$ mm and $\Phi = 190°$

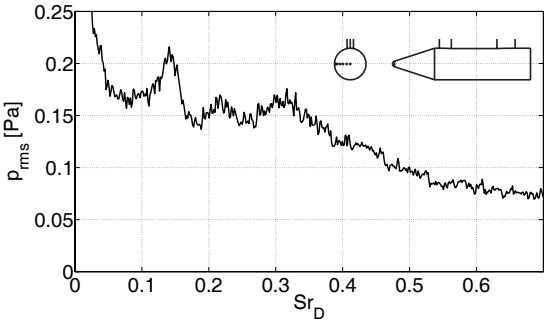

(b) Location: $r = 45$ mm and $\Phi = 270°$

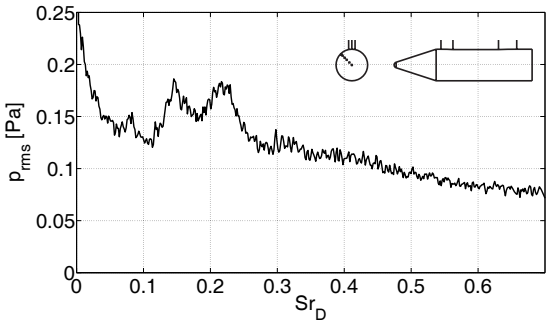

(c) Location: $r = 45$ mm and $\Phi = 315°$

Figure 17: Experimental pressure spectra at different azimuthal locations without a nozzle extension

The pressure transducers on the base were used to gain further insight into the unsteady nature of the recirculation zone. The pressure spectra for various positions on the base are given in Fig. 17 and Fig. 18, whereas the first one delivers a detailed view on the dominant Strouhal numbers and the latter intends to give a spacial impression of the pressure fluctuations on the base. Fig. 18 contains the data of Fig. 17.

The pressure spectrum at three outer azimuthal locations ($\Phi = 180°, 270°$ and $315°$) with about the same radial distance ($r = 40$ and 45 mm) for the configuration without a nozzle extension is given in Fig. 17. Independent to the azimuthal location, the three pressure transducer feature a dominant Strouhal number at about $Sr_D = 0.21 - 0.22$ and some pressure fluctuations seem to oscillate with a broader frequency, which centers around $0.31 - 0.33$. Additional non-dimensional frequencies can be detected at $Sr_D = 0.08 - 0.09$ ($\Phi = 180°$ and $315°$) and a strong signal at $Sr_D = 0.145$ ($\Phi = 180°$ and $270°$). These graphs were chosen to show exemplarily the reoccurring non-dimensional frequencies of $Sr_D = 0.08 - 0.09, 0.145, 0.21 - 0.22$ and about $0.31 - 0.3$.

As an additional information to the graphs before, Fig. 18(a) to Fig. 18(d) depict the radial distance according to the pressure transducer arrangement introduced in Fig. 7 for $\Phi = 180°, 225°, 270°, 315°$. Taking all four graphs into consideration, it can be observed that the level of the pressure fluctuations increases continuously towards the center of the base and oscillate with a dominant frequency of $Sr_D = 0.08$. Towards the outer region, a dependency to the azimuthal location can be detected. Whereas the same non-dimensional frequency are detected for the transducers at $r = 12$ and 25 mm, it can be denoted that additional frequencies appear in the pressure spectrum. For example, the transducers at $\Phi = 225°, 270°, 315°$ measure fluctuations with a Strouhal number of about $Sr_D = 0.145$. This frequency is also part of the spectra for the outer sensors at $r = 35, 45$ and 50 mm at the same azimuthal location. Even more dominant non-dimensional frequencies join the pressure spectra when approaching the outer region of the base. As it was discussed in the detailed examination of Fig. 17, the outer transducer exhibit additional frequencies at about $Sr_D = 0.21 - 0.22$ and a broad-band signal centering at about $0.31 - 0.33$ in the pressure spectra. Meanwhile, the fluctuations at the center Strouhal number of 0.08 almost completely disappear. A note concerns the distinct peaks of the transducers at $r = 35$ and 45 mm: these peaks are most likely caused by electro-magnetic interferences since they are independent to experimental input conditions.

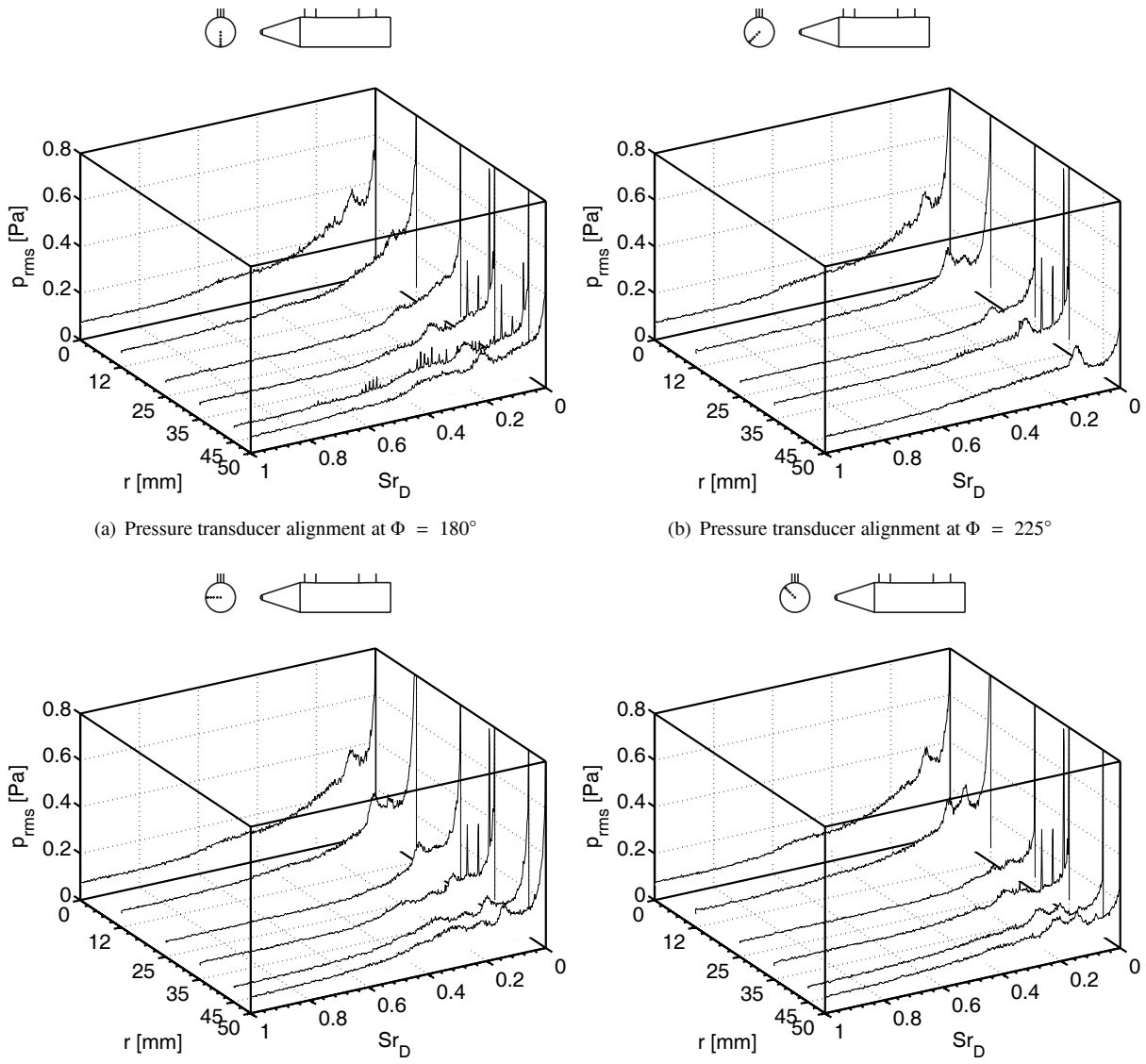

(a) Pressure transducer alignment at $\Phi = 180°$

(b) Pressure transducer alignment at $\Phi = 225°$

(c) Pressure transducer alignment at $\Phi = 270°$

(d) Pressure transducer alignment at $\Phi = 315°$

Figure 18: Pressure spectra for radial pressure transducer alignment at different angles Φ

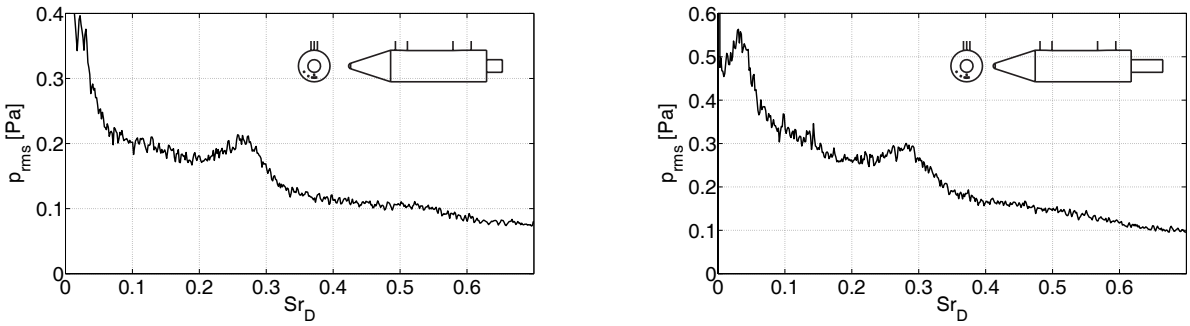

(a) Nozzle extension length of $L/D = 0.5$.

(b) Nozzle extension length of $L/D = 1.0$.

Figure 19: Experimental pressure spectra for different nozzle lengths at $r = 40\,\text{mm}$ and $\Phi = 190°$

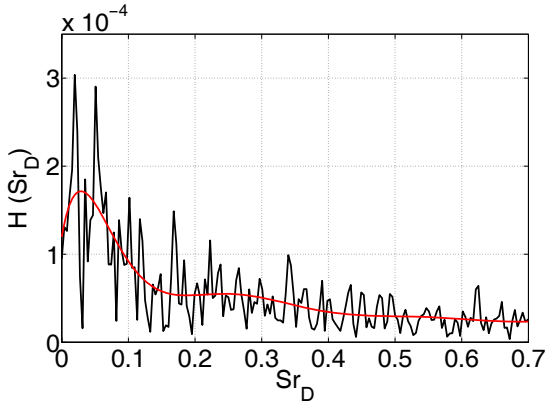

Figure 20: Numerical pressure spectra at the position $r = 40\,\text{mm}$ determined

The influence of a nozzle attached to the end of the generic launcher on the pressure fluctuations is discussed in the following. The data is presented in the same manner as before. A single pressure spectrum is extracted from the graphs that show the spacial distribution and is then discussed in detail.

Fig. 17(a), Fig. 19(a) and Fig. 19(b) show the pressure spectra at $r = 40\,\text{mm}$ and $\Phi = 190°$ for the configuration without a nozzle, with a nozzle attachment of the length $L/D = 0.5$ and $L/D = 1.0$, respectively. It can clearly be seen that the pressure spectrum undergoes a crucial change. For the configuration without a nozzle extension, several dominant Strouhal number were identified at about 0.08, 0.21 - 0.22 and 0.31 - 0.33. The pressure spectrum for both nozzle extension are very similar. It features a peak at about $0.025 - 0.03$ and another distinct Strouhal number at about 0.27.

The pressure fluctuations for configuration B (Fig. 20) were also extracted at the corresponding location at $r = 40\,\text{mm}$. A 10^{th}-order polynomial is fitted through the spectra in order to receive the trend. As it can be seen, the course of the polynomial features a peak at a low non-dimensional frequency at about $Sr_D = 0.03$ and some broad-band fluctuations at about 0.27. Overall, the course of the polynomial resembles the course of the pressure spectra found in experiments (Fig. 19(b)).

The spacial distribution of the pressure fluctuations when a nozzle is added to the base is given in Fig. 21 for the transducer arrangement described in Fig. 8. The spacial direction in the graphs here represent the azimuthal position Φ at $r = 40\,\text{mm}$. Fig. 21(a) contains data of the already discussed pressure spectrum in Fig. 17(a) with distinct pressure fluctuations Strouhal numbers at about $0.08-0.09$, $0.21-0.22$ and 0.31-0.33. The transducers in the clockwise direction towards the strut show mainly the same Strouhal numbers except that frequency contents especially at 0.21- 0.22 get damped.

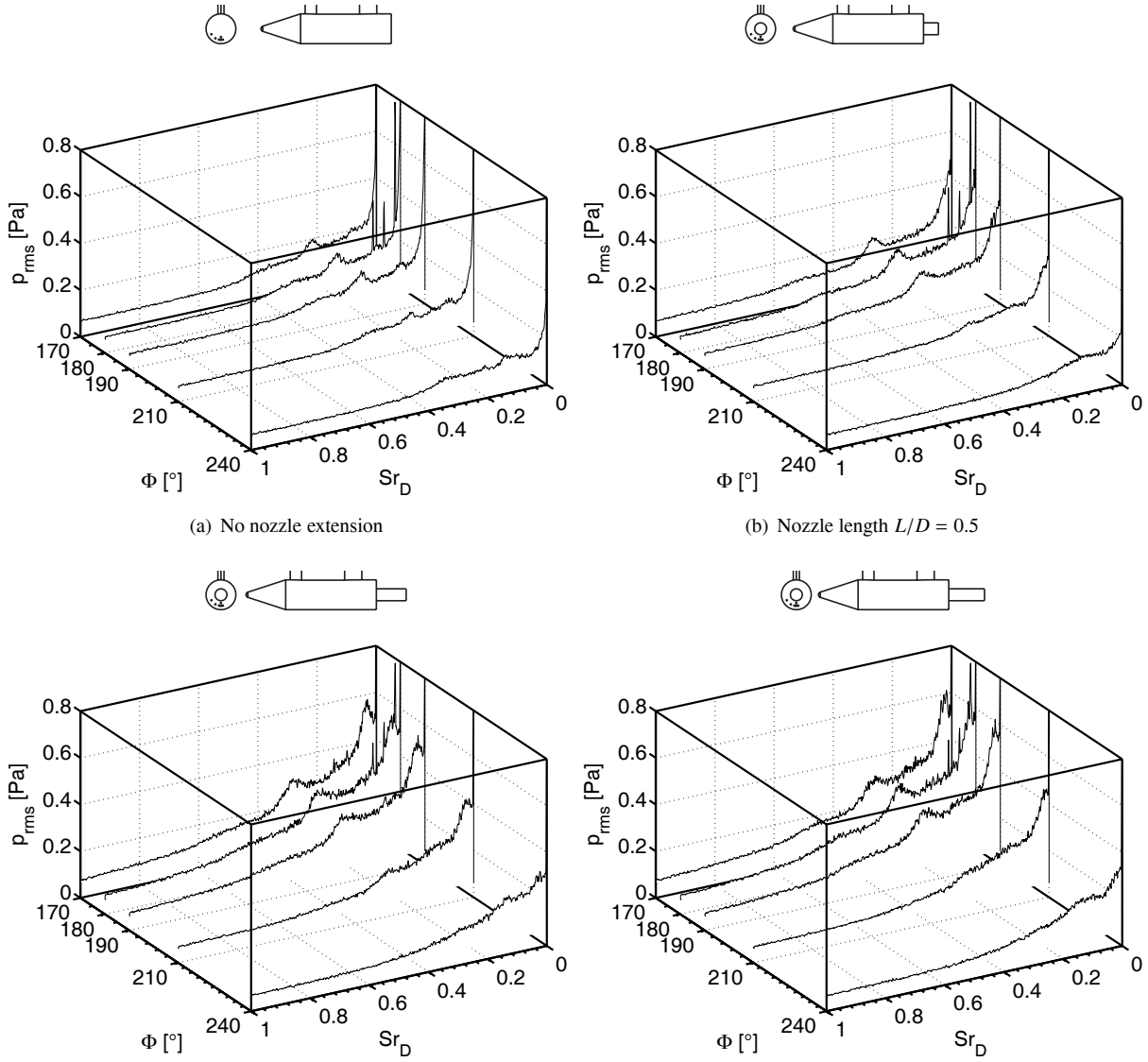

(a) No nozzle extension

(b) Nozzle length L/D = 0.5

(c) Nozzle length L/D = 1.0

(d) Nozzle length L/D = 1.2

Figure 21: Experimental pressure spectra for different nozzle extension lengths at $r = 40\,\mathrm{mm}$

The short nozzle attachment with $L/D = 0.5$ now results in a change in the dominant Strouhal number to $Sr_D = 0.27$ (Fig. 21(b)) and some high pressure fluctuations at low frequencies with no distinct peak. Other frequency contents can not be detected anymore. The non-dimensional frequency of 0.27 is most distinct on the opposite side of the strut, and as seen before in Fig. 21(a), smears out to a broadband signal for the transducers closer to the strut. Along with the frequency shift comes an increase of the pressure fluctuation level.

The tendency in the pressure spectra that was observed with the attachment of a nozzle continues with the even longer nozzle extension with $L/D = 1.0$. Fig. 21(c) shows an overall increase of the pressure level, fluctuations at the distinct Strouhal number 0.27 and a broader signal for the transducers in the clockwise direction towards the strut. Additionally, the low frequency fluctuations now feature a distinct peak at about $0.025 - 0.03$. A further lengthening of the nozzle extension to $L/D = 1.2$ does not influence the pressure spectra on the base anymore. The course of the spectra in Fig. 21(c) and Fig. 21(d) are practically identical.

4. Discussion

After a short discussion about the forebody and the state of the boundary layer, this part continues with the interpretation of the unsteady effects in the recirculation zone and focuses on the crucial differences between a free reattachment of the flow in comparison to a reattachment on a solid surface after the shoulder expansion.

The measurements results of the Pitot pressure (Fig. 12) and the infrared image (Fig. 11) before the base both indicate that the boundary layer is not fully laminar. The course of the Pitot pressure in the radial direction coincides with the calculated laminar course close to the wall and resembles the turbulent boundary layer further away from the surface. This ambiguous interpretation is supported by the infrared images. The temperature transition evidence a laminar-turbulent transition, and it can be seen that the strut actually triggers transition at the upper part of the main body, but for the lower part of the cylinder, this transition can not be observed. Nevertheless, despite the ambiguous information from the incoming boundary along the main body, the investigated case shows strong similarities to the case described in reference [12] with a turbulent boundary layer and a Reynolds number of $16 \cdot 10^6\,\mathrm{m}^{-1}$ and comparisons will be drawn later in this section. The pattern with higher temperature on the surface in the streamwise direction is attributed to the footprint of the shock and the expansion from the strut.

The pressure spectra reveal that the internal flow dynamics and the flow topology of the recirculation zone undergoes a crucial change when a nozzle is attached to the end. On the other side, the external flow outside of the recirculation zone is not influenced by the internal flow dynamics. Hence, the results indicate that no conclusions to the flow dynamics of the recirculation zone can be drawn from the behavior of reattachment shock, and that these two effects are independent to each other.

In detail, this hypothesis is backed by the observation that the recompression shock is shifted parallelly upstream to the base when a nozzle is attached (Fig. 13), while the oscillation of this shock takes place with the same non-dimensional frequency of about 0.18-0.19 (Fig. 15). The pressure spectra inside the recirculation zone instead features pressure spectra that can not directly be related to the spectra of the recompression shock location. This statement is even supported by the numerical investigations. Although the location of the recompression shock is calculated to be further downstream than measured in experiments (Fig. 14), meaning that the shape of the recirculation zone is larger, the polynomial of the shock location spectra still returns a peak at the same Strouhal number 0.19.

In literature, a Strouhal number of about 0.2 is often related to the flapping motion of the von Kármán vortex street caused by the unsteady separation of the flow from a blunt body. But, the issue of transferring this idea to the problem at hand lays in the fact that splitter plates or fins suppress and delay the flapping motion. The nozzle extension can be seen as such a device. Hence, another effect might also play a role in the unsteady behavior of the reattachment shock.

It seems that the crucial change of pressure fluctuation in the recirculation zone can be related to flows with free reattachment and with reattachment on a solid wall. The pressure spectra of the two different configurations differ in the number of distinct peaks, the non-dimensional dominant frequencies and the level of the pressure fluctuations.

The number of distinct peaks that can be detected in the pressure spectra in Fig. 18(a) to 18(d) indicate more modes for the flow with free reattachment. Dominant Strouhal numbers were detected at 0.08-0.09, 0.145, 0.21-0.2 and at between 0.31 and 0.33. The link to a overarching vortex motion based on the spectra only is difficult. In literature, fluctuations with a periodicity of 0.08-0.09 for example are often related an axisymmetric growth and decay process of the recirculation zone and, as mentioned before, the periodicity of 0.2 is connected to the von Kármán vortex shedding. More research has to be done to identify fluid motions that oscillate with the Strouhal numbers of 0.145 and at about 0.32. A common feature that can be observed in all spectra concerns the low pressure fluctuations close to the edge of the base, which intensify towards the center of the base where it reaches a maximum peak. This effect might be due focussing pressure fluctuations emanating circumferentially from the shear layer. Further, it can be seen that there is an azimuthal dependency of the pressure fluctuations, which give rise to the idea of azimuthal pressure modes seen in [8]. On the other hand, it can not be stated without doubt that a preferred orientation is introduced by the strut since the transducers 10° left and right from the strut are comparable.

Fig. 13 shows an identical location for the recompression shock for the nozzle extension of $L/D = 1.0$ and 1.2. This suggests that the recirculation region is identical as well and, hence the same pressure spectra should be an outcome of this finding. This can be seen in the striking similarity of Fig. 21(c) and 21(d). The flow reattaches for both cases on a solid wall and simplifies the flow dynamic in a sense that only two dominant Strouhal number can be detected at about $0.025 - 0.03$ and 0.27. An explanation to the reduction of the amount of distinct frequencies might be that the application of the nozzle extension influences the recirculation zone in such a way that only symmetric effects like the growth and decay of the recirculation region or the varicose mode shedding from the shoulder play a role in the dynamics. It seems obvious that antisymmetric movements are somehow suppressed. Additionally, the results of

the numerical simulations concerning the agreement of the pressure spectra (Fig. 20) justifies the comparison between configuration A with a nozzle extension and B.

A special case is considered for the nozzle extension of $L/D = 0.5$. The fact the recompression shock does not coincide with the shocks of the longer nozzles (Fig. 13) means that the flow is not completely reattached. Yet, a recompression with a realignement of the flow takes place on the nozzle extension, where the flow is deviated in the axisymmetric direction. This is where a first shock is formed. At the rear end of the nozzle, the flow is deviated towards the axis again and must finally undergo another recompression, where further recompression waves emanate. The two shocks interact the position where the kink is located. The angle of the first shock is lower since the reattachment or realignment on the nozzle is most likely not complete. Consequently, the recirculation region is not identical to the one with the longer nozzles and different pressure spectra can be observed (Fig. 21(d)). The dominant Strouhal number of 0.27 can also be found. But, there is no distinct low frequency fluctuation at 0.025 – 0.03 and the overall pressure level is lower.

The investigations at hand reveal striking similarities to reference [12], which were carried out on the same model at a unit Reynolds number $16 \cdot 10^6\,\mathrm{m}^{-1}$ and at Mach 6.0. For the free reattachement of the flow, comparable features like a maximum in the pressure fluctuations at $Sr_D = 0.08$ in the center of the base could be found as well. Closer to the edge of the base, the former experiments also showed a distinct peak at Strouhal number 0.2. In contrast to the experiments here, no peaks were found at $Sr_D = 0.145$ and at between 0.31 and 0.33. The former experiments measured a peak at 0.38 instead. The fluctuations of the recompression shock were identical. This indicates that the recompression shock and the fluctuations that take place at 0.08 and at approximately 0.2 seem to be independent to the Reynolds number and the incoming boundary layer. Vice versa, this might mean that some fluctuations show a sensitivity to criteria mentioned before. For the case here, incoming boundary layer or Reynolds number seems to be the reason for fluctuations at 0.145 and at broadband signal at about 0.32 for the free reattachment of the flow.

The reattachement of the flow on a solid wall for $Re_U = 16 \cdot 10^6\,\mathrm{m}^{-1}$ follows the same pattern as for the current investigations. In both cases, a distinct peak at $Sr_D = 0.27$ can be observed and the recompression shock oscillates in the vertical direction with a Strouhal number of 0.2. The mean recompression shock differs location though. It is shifted closer to the axis and the shock angle is steeper than from the case with $Re_U = 10 \cdot 10^6\,\mathrm{m}^{-1}$. Consequently, the deviation of the flow from the shoulder is even larger there.

5. Conclusion

In the present paper, axisymmetric base flows at $Ma = 6.0$ at a Reynolds number of $10 \cdot 10^6$ were investigated experimentally for different nozzle extensions and compared to the numerical results from the zonal RANS/LES method applied on the geometry with a sting support. Measurements on the forebody by means of a Pitot rake and thermography have been conducted to provide information about the boundary layer at the rear end of the main body. The base flow was studied by measuring the unsteady base pressure fluctuations complemented with the data from unsteady high-speed schlieren measurements. At the corresponding locations, measurement data and results from the numerical simulations were compared to each other.

On the one hand, the measurement revealed that the wake flow is divided into the external flow that is not directly coupled with the internal flow of the recirculation region. The recompression shock oscillates independently with a Strouhal number of $Sr_D = 0.18$-0.19 without or with nozzle attachments. On the other hand, it was also shown that the dynamics of recirculation region is heavily influenced by the reattachment of the flow. For a free reattachment, dominant Strouhal number could be measured at 0.08-0.09, 0.145, 0.21-0.22 and at about 0.32. For the blunt base configuration, the pressure fluctuations focus to a peak pressure level at 0.08-0.09 in the center of the base. For a reattachment on a solid surface, the pressure fluctuations measured before are suppressed and peaks at 0.025-0.03 and at 0.27 occur.

The applied zonal RANS/LES method has been demonstrated to predict satisfactorily the intricate wake flow for high Reynolds numbers. Although the mean location for the recompression flow differs from the experimental results, the dynamic behavior of the flow is reproduced for the configuration with sting support. For the recompression shock, a dominant Strouahl number of 0.18 was calculated and the pressure fluctuations feature a periodicity of 0.03 and 0.27, which is identical to the experimental results.

Due to the difficulties of attributing flow phenomena to certain frequencies, future work from the experimental point of view will focus on a higher spacial resolution of the base pressure fluctuations. Further, the measurement method of particle image velocimetry will be applied to gain more insights into the mean flow topology, the shear layer and the turbulent velocity. The numerical investigations can certainly be used to narrow down the driving mechanisms

concerning interaction of the external flow and the recirculation region.

Acknowledgement

Financial support has been provided by the German Research Foundation (Deutsche Forschungsgemeinschaft - DFG) in the framework of the Sonderforschungsbereich Transregio 40. The help and advice of the technical stuff of the supersonic and hypersonic department is gratefully acknowledged. A data acquisition system has been kindly provided by the Institute of Aeronautics and Astronautics, RWTH Aachen.

References

[1] Boris, J.P., Grinstein, F.F., Oran, E.S., Kolbe R.L. 1992. New insights into large eddy simulation. Fluid Dynamics Research, Vol. 10(4-6), pp. 199-228.

[2] Fureby, C., Grinstein, F.F. 2002. Large Eddy Simulations of High-Reynolds-Number Free and Wall-Bounded Flows. J. Comp. Physics, Vol. 181, pp. 68-97.

[3] Jarrin, N., Benhamadouche, N., Laurence, S., Prosser, D. 2006. A synthetic-eddy-method for generating inflow conditions for large-eddy simulations. J. Heat and Fluid Flow, 27, pp. 585-593.

[4] Keating, A., de Prisco, G., Piomelli, U. 2006. Interface conditions for hybrid RANS/LES calculation. International Journal of Heat and Fluid Flow, Vol. 27, pp. 777-788.

[5] König, D., Meinke, M., Schröder, W. 2010. Embedded LES/RANS Boundary in Zonal Simulations. J. of Turbulence, Vol. 11, pp. 1-25.

[6] van Leer, B. 1979. Towards the Ultimate Conservative Difference Scheme V. A Second-Order Sequel to Godunov's Method. J. Comp. Physics, Vol. 32, pp. 101-136.

[7] Liou, M.S., Steffen, C.J. 1993. A New Flux Splitting Scheme. J. Comput. Phys., Vol. 107, pp. 23-39.

[8] Meiss, J.-H. and Schröder, W. 2007. Large-Eddy Simulation of a Generic Space Vehicle. In: A. Gülhan (ed.), RESPACE - Key Technologies for Reusable Space Systems, Springer-Verlag Berlin Heidelberg, ISBN 978-3-540-77818-9, pp. 21–39, 2008.

[9] Neeb, D. 2007. Experimentelle Untersuchung der Heckströmung einer Boosterkonfiguraion im Hyperschall. Diplomarbeit at the German Aerospace Center, Institute of Aerodynamics and Flow Technology, Supersonic and Hypersonic Technology Department, Cologne.

[10] Ottens, H.B.A., M.I. Gerritsma, W.J. Bannink. 2001. Computational Study of Support Influence on Base Flow of a Model in Supersonic Flow. AIAA Paper 2001-2638.

[11] Rollstin, L. 1987. Measurement of inflight base-pressure on an artillery-fired projectile. AIAA Paper 287-2427.

[12] Saile, D., Gülhan, A., Henckels, A. 2011. Investigations on the Near-Wake Region of a Generic Space Launcher Geometry. 17^{th} AIAA International Space Planes and Hypersonic Systems and Technologies Conference, Manuscript ID #947684.

[13] Spalart, P.R., Allmaras, S.R. 1992. A One-Equation Turbulence Model for Aerodynamic Flows. AIAA Paper 92-0439.

[14] Spille, A., Kaltenbach, H.-J. 2001. Generation of turbulent inflow data with a prescribed shear-stress profile. Third AFSOR Conference on DNS and LES.

[15] Zhang, Q., Schröder, W., Meinke, M. 2010. A zonal RANS-LES method to determine the flow over a high-lift configuration. Computers and Fluids, Vol. 39, Issue 7, pp. 1241-1253.